Ultralow-voltage hydrogen production and simultaneous pollutant recycling in neutral media

Xiang Peng[1,2], Song Xie[1], Shijian Xiong[1], Rong Li[1], Peng Wang[1], Zhitian Liu[1,*], Xuming Zhang[3], Liangsheng Hu[4], Biao Gao[2,3,*], Paul K. Chu[2,*]

[1] Hubei Key Laboratory of Plasma Chemistry and Advanced Materials, Hubei Engineering Technology Research Center of Optoelectronic and New Energy Materials, School of Materials Science and Engineering, Wuhan Institute of Technology, Wuhan, 430205, China

[2] Department of Physics, Department of Materials Science and Engineering, Department of Biomedical Engineering, City University of Hong Kong, Tat Chee Avenue, Kowloon, Hong Kong, China

[3] State Key Laboratory of Refractories and Metallurgy and Institute of Advanced Materials and Nanotechnology, Wuhan University of Science and Technology, Wuhan, 430081, China

[4] Department of Chemistry and Key Laboratory for Preparation and Application of Ordered Structural Materials of Guangdong Province, Shantou University, Guangdong, 515063, China

Correspondence: able.ztliu@wit.edu.cn (Z. Liu), gaobiao@wust.edu.cn (B. Gao), paul.chu@cityu.edu.hk (P.K. Chu)

Abstract:

Electrocatalytic water splitting for hydrogen production is hampered by the sluggish oxygen evolution reaction (OER) and large power consumption and replacing the OER with thermodynamically favorable reactions can improve the energy conversion efficiency. Since metal atoms reconstruct and generate oxidation currents before OER on transition metal-based electrocatalysts, a novel strategy to integrate the hydrogen evolution reaction (HER) with waste Fe upgrading reaction (FUR) is proposed and demonstrated for energy-efficient hydrogen production in neutral media. The heterostructured $MoSe_2/MoO_2$ on carbon cloth (MSM/CC) shows superior HER performance to that of commercial Pt/C at high current densities. By replacing conventional OER with FUR, the potential required to afford 10 mA cm^{-2} decreases by 95%. The HER/FUR overall reaction shows an ultralow voltage of 0.68 V for 10 mA cm^{-2} with a power equivalent of 2.69 kWh per m^3 H_2. In addition to energy-saving hydrogen production, the Fe species formed at the anode extract the Rhodamine B (RhB) pollutant by flocculation and also produce nanosized magnetic powder and beneficiated RhB for value-adding applications. This work demonstrates both energy-saving hydrogen production and pollutant recycling by a single system and reveals a new direction to integrate hydrogen production with environmental recovery to achieve carbon neutrality.

Keywords: energy-saving hydrogen production, hydrogen evolution reaction, neutral water splitting, zero-carbon emission, environmental recovery

1. Introduction

Electrochemical water splitting driven by sustainable energy is one of the promising techniques to produce high-purity hydrogen in the global efforts to replace fossil fuels and achieve carbon neutrality [1-4]. The efficiency of hydrogen production depends on the physicochemical and electrochemical properties of the electrocatalytic couples and electrocatalysts [5, 6]. Electrochemical water splitting consists of the hydrogen evolution reaction (HER) on the cathode and oxygen evolution reaction (OER) on the anode. OER is considered the rate-determining step due to the large theoretical potential barrier ($4OH^- \rightarrow O_2 + 2H_2O + 4e^-$, 1.23 V *vs*. RHE) in addition to a big overpotential, thus entailing high electricity consumption [7]. Therefore, developing a thermodynamically easier and less energy-demanding reaction to replace OER is critical.

Recently, thermodynamically favorable oxidation of small molecules and organic species electro-oxidative reactions have been integrated to produce hydrogen by HER [8-13]. For instance, Qian et al. have utilized hydrazine oxidation to replace OER and the two-electrode electrolyzer requires cell voltages of 0.071 and 0.76 V for 10 and 400 mA cm^{-2}, respectively [14]. The combination of electrooxidation of organic pollutants and HER in a single system is a promising solution for the simultaneous treatment of wastewater and renewable energy generation [15-17]. Sun et al. have demonstrated hydrogen production by hybrid seawater splitting coupled with hydrazine degradation, which presents a low electricity equivalent of 2.75 kWh per m^3 H_2, thus enabling hydrogen production and removal of harmful pollutants at the same time [18]. These strategies have been shown to improve the energy efficiency of hydrogen production but nevertheless, the gaseous products either need purification or contribute to carbon emission. Moreover, the kinetics of HER and anodic reactions must match in order to improve the Faradaic efficiency in overall water splitting.

To attain zero carbon emission and energy-saving hydrogen production, it is desirable to develop an anodic oxidation reaction which is thermodynamically easier than OER and has

high synergism. Transition metal-based electrocatalysts undergo reconstruction before OER, during which, metal atoms with a low valance state are oxidized to a higher valancy to produce an oxidation current with thermodynamic favorability [19-21]. Hence, it is possible that the reconstruction process in the metal oxidation reaction can replace OER and be coupled with HER to enhance overall water splitting. However, this strategy has seldom been reported so far, perhaps because metal oxidation consumes the anode, consequently raising the operating and materials costs. Electrochemical flocculation has been used in environmental fields to remove pollutants including heavy metal ions and organic species in pH-neutral wastewater. It proceeds at a positive potential *via* the Fe oxidation reaction to form the flocculant (hydroxy complex, polynuclear hydroxy complex, and hydroxide) [22]. In addition, Fe tends to self-corrode and forms magnetic oxide species (Fe upgrading reaction, FUR), even though applying a very small positive potential can facilitate FUR [23, 24]. Therefore, integrating HER at the cathode and FUR at the anode may result in highly efficient hydrogen production. However, the design and construction of high-performance HER electrocatalysts for neutral water splitting are still challenging.

Despite the excellent HER capability of Pt- and Ru-based noble catalysts[25-27], more cost-effective candidates such as metal carbides [28-30], metal phosphides [31, 32], metal sulfides [33, 34], metal nitrides [35-37], and metal selenides [38, 39] are being explored as replacements. In particular, two-dimensional layered molybdenum selenides ($MoSe_2$) have attracted much attention due to the favorable hydrogen adsorption free energy (ΔG_H) and tunable active sites [40, 41]. $MoSe_2$ normally exists in the 1*T* and 2*H* phases. 2*H*-$MoSe_2$ is an indirect bandgap semiconductor with low electrical conductivity, whereas 1*T*-$MoSe_2$ has metallic behavior and better HER capability, albeit poorer stability [42]. Qu et al. have prepared the Mo/(1*T*-2*H*)-$MoSe_2$ composite, which shows a small Tafel slope of 35 mV dec^{-1} and good stability [43]. Deng et al. have constructed the bi-phase (1*T*-2*H*)-$MoSe_2$ on a conductive substrate and shown a small overpotential of 126 mV to achieve 10 mA cm^{-2} [44]. Therefore,

2*H*-$MoSe_2$ as the substrate can facilitate modification of the electronic structure of 1*T*-$MoSe_2$, which serves as the main active center in the (1*T*-2*H*)-$MoSe_2$ electrocatalyst. However, $MoSe_2$ is oxidized quite easily, consequently compromising the long-term stability. Nevertheless, combining electrochemically active 1*T*-$MoSe_2$ with highly conductive and stable Mo-based oxides may be a good strategy to produce highly active and stable composite electrocatalysts.

Herein, we propose to realize energy-saving and efficient hydrogen production by a combined water splitting and pollutant extracting strategy in a neutral electrolyte. In the process, electrolysis of neutral water on the cathode produces high-purity hydrogen *via* HER, while Fe is converted into Fe^{2+} at the anode *via* FUR instead of OER. HER is catalyzed by the heterostructured $MoSe_2/MoO_2$ composite prepared on carbon cloth (MSM/CC) produced by *in situ* phase separation. Fe^{2+} generated on the anode forms the $Fe(OH)_2$ to adsorb Rhodamine B (RhB, a typical and soluble dye molecule applied in a variety of industries) by flocculation to facilitate wastewater treatment. Meanwhile, magnetic Fe_3O_4 nanoparticles are produced. All in all, the dual process produces hydrogen and remove RhB pollutant at the same time without carbon emission, as schematically illustrated in **Scheme 1**. The HER/FUR couple requires 0.68 V to generate a current density of 10 mA cm^{-2} and can be powered by solar cells with an electricity equivalent of 2.69 kWh per m^3 H_2. The results reveal a new direction to realize energy-efficient hydrogen production in neutral media with zero-carbon emission and environmental recovery at the same time.

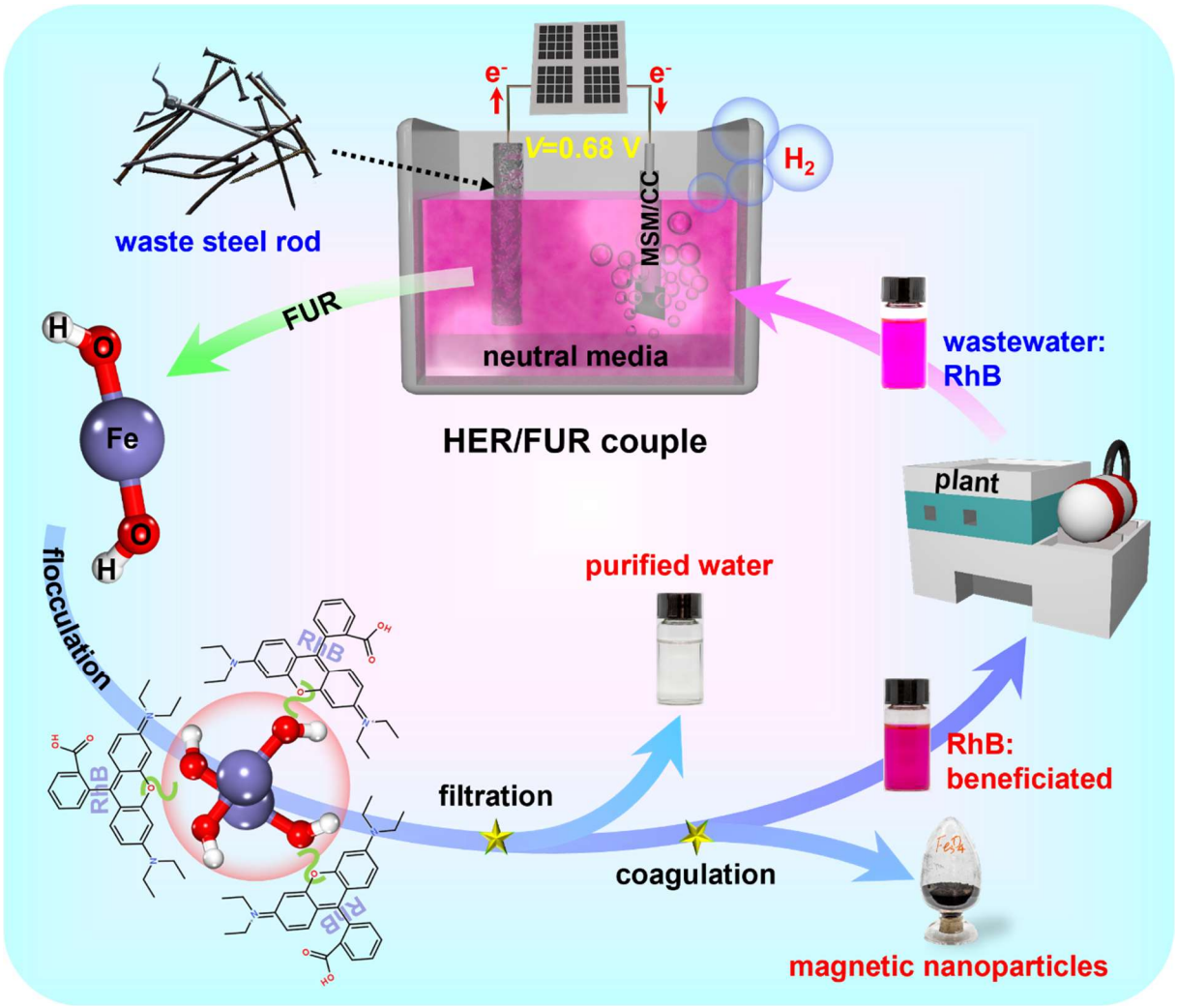

Scheme 1. Schematically illustration of the concept of HER/FUR couple for ultralow-voltage hydrogen production and simultaneous magnetic Fe_3O_4 nanoparticles production, wastewater purification as well as RhB beneficiation in neutral media.

2. Experimental Section/Methods

Synthesis of MoO_3/CC: The MoO_3 nanowire arrays were grown on carbon cloth (CC) by a solution method. In detail, 0.9 g of $(NH_4)_2MoO_4$·were added to a solution (50 mL) of HNO_3 and deionized water (DW) with a volume ratio of 4:1. A piece of clean CC (2 × 3 cm^2) was immersed in the solution and then heated to 70 °C for 1 h in a water bath. The product was CC covered by MoO_3 nanowires (MoO_3/CC).

Synthesis of MSM/CC: The $MoSe_2/MoO_2$ core-shell structure was prepared by CVD. MoO_3/CC and 1 g of Se powder were put on two separate porcelain plates with the Se powder upstream in the tube furnace. MoO_3/CC was heated to 400 °C for 1 h at a ramping rate of 5 °C min^{-1} under N_2/H_2 (containing H_2 of 8%) and then cooled to room temperature. The product was designated as MSM/CC.

Synthesis of $MoSe_2$/CC and MoO_2/CC: Pure $MoSe_2$ was prepared by CVD similar to that for MSM/CC except that the temperature was 500 °C. The product was designated as $MoSe_2$/CC. Pure MoO_2 was prepared by hydrogen reduction, in which MoO_3/CC was put in a tube furnace, heated to 550 °C for 3 h under N_2/H_2 (containing H_2 of 8%), and cooled to room temperature. The product was designated as MoO_2/CC.

Materials characterization: The morphology and composition of the samples were characterized by field-emission scanning electron microscopy (FE-SEM, TESCAN MIRA LMS), transmission electron microscopy (TEM, FEI F200), high-resolution TEM (HR-TEM) equipped with energy dispersive X-ray (EDX) spectroscopy, X-ray diffraction (XRD, LabX XRD-6100, Shimadzu) with a Cu K_α source, and Raman scattering (HR RamLab). X-ray photoelectron spectroscopy (XPS, Thermo Scientific K-Alpha+, Thermo Fisher) with monochromatic Al K_α X-rays was performed to determine the chemical state of the samples and the binding energy of 284.6 eV of C 1*s* was the reference. The electrical conductivity was evaluated by a four-point probe using the Keithley 2450. The magnetic properties were investigated on the vibrating sample magnetometer (Lakeshore 7404). The total organic carbon (TOC) in the electrolyte was measured by a carbon analyzer (Elementar Vario TOC) and the UV-vis spectra were acquired from the PerkinElmer Lambda 35.

Electrochemical characterization: The electrochemical measurements were carried out based on the three-electrode configuration on the CHI 760E (Shanghai CH Instrument, China). The reference and counter electrodes were the saturated calomel electrode (SCE) and graphite rod, respectively. The CC modified with the nanostructures served as the working electrodes. A

typical waste steel rod used for construction was used as the working electrode (anode) in FUR (overall reaction). All the potentials in HER were *iR* corrected and calibrated to the reversible hydrogen electrode (RHE) by the Nernst equation $E(\text{RHE}) = E(\text{SCE}) + 0.242 + 0.059 \times \text{pH}$, where the pH values of 0.5 M H_2SO_4, 1.0 M KOH, and 0.5 M Na_2SO_4 were 0.48, 13.58, and 5.80 (FE28, Mettler Toledo), respectively. Linear sweep voltammetry (LSV) was conducted at a scanning rate of 5 mV s^{-1} and the Tafel slope was calculated from the linear portion of the Tafel plot. Electrochemical impedance spectroscopy (EIS) was performed with an amplitude of 5 mV in the frequency range of 100 kHz ~ 0.1 Hz. The electrochemically active surface area (ECSA) was determined by cyclic voltammetry (CV) in the potential range between –0.5 and –0.6 V *vs*. SCE. The HER stability was determined at a potential of –1.4 V *vs*. SCE and the amount of H_2 produced was measured by the water displacement method.

3. Result and discussions

Figure S1 illustrates the preparation of the core-shell $MoSe_2/MoO_2$ composite. The MoO_3 nanowires are grown on the carbon cloth (MoO_3/CC) by a solution method and then phase-separated to form the core-shell $MoSe_2/MoO_2$ on CC (MSM/CC). The surface morphological evolution during phase separation is schematically presented in **Figure 1a** and confirmed by morphological characterization. The field-emission scanning electron microscopy (FE-SEM) images in **Figures S2a-b** show that the uniform nanowire array with a smooth surface covers the carbon fibers. After CVD for selenation, the nanowire array structure remains, but the surface becomes rough and sheet-like (**Figures 1b-c**). In addition, the diameter of the nanowires increases distinctly. By increasing the CVD temperature to 500 °C, similarly rough nanowire arrays are still obtained as shown in **Figure S3**. Hence, nanosheets are formed on the surface of the nanowires after selenation. After annealing the MoO_3/CC in the same atmosphere but without the Se precursor, the nanowire structure can still be observed as shown in **Figure S4**.

The transmission electron microscopy (TEM) images in **Figure S5** and **Figure 1d** confirm the nanosheet-nanowire core-shell structure of the CVD product with a core diameter of ~200 nm and a shell diameter of ~400 nm, in line with SEM analysis. The nanosheet structure is beneficial for active site exposure for fast catalysis. **Figure 1e** indicates firm integration between the nanowire core and nanosheet shell without sharp boundaries. Furthermore, the high-resolution TEM (HR-TEM) image in **Figure 1f** shows two sets of distinct lattice fringes with a neighboring distance of 0.24 nm of the nanowire core ascribed to the MoO_2 (–211) plane (JCPDS card No. 32-0671), whereas the lattice of 0.65 nm of the nanosheet shell belongs to the $MoSe_2$ (002) plane (JCPDS card No. 77-1715). The elemental maps in **Figure 1g** disclose the Mo-O core and Mo-Se shell in the as-prepared MSM.

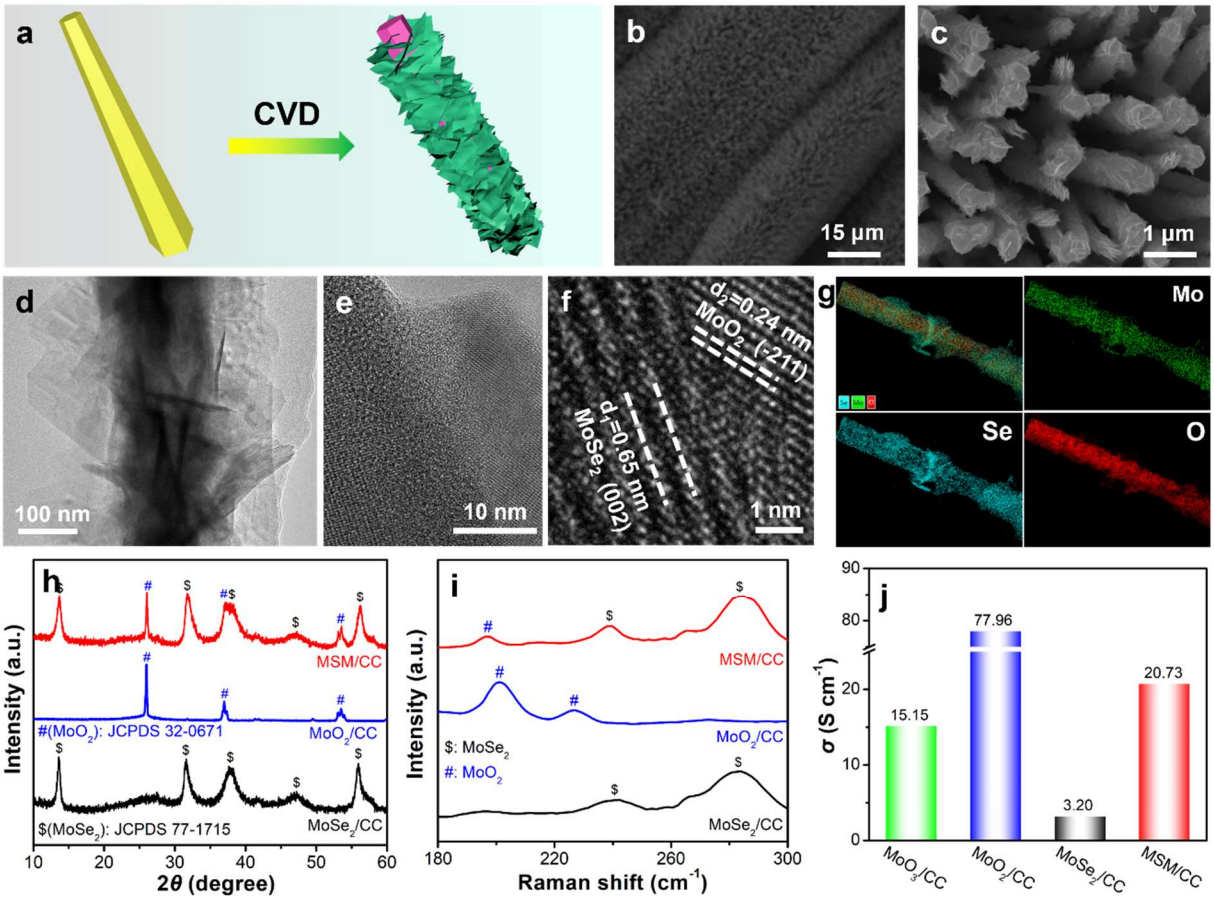

Figure 1. (a) Schematic of the conversion of the MoO_3 nanowire into MSM core-shell structure; (b-c) FE-SEM and (d-e) TEM images of MSM/CC; (f) HR-TEM image and (g) Elemental maps

of MSM/CC; (h) XRD spectra, (i) Raman scattering spectra, and (j) Electrical conductivity of the electrocatalysts.

The X-ray diffraction (XRD) pattern in **Figure S6** shows that the product formed by the solution process is MoO_3 (JCPDS card No. 21-0569). After CVD for selenation at 400 ^oC, **Figure 1h** indicates that the diffraction patterns (red line) of the product belong to the composite of $MoSe_2$ (JCPDS card No. 77-1715) and MoO_2 (JCPDS card No. 32-0671). The results confirm that MoO_3 is phase-separated into the composite of $MoSe_2$ and MoO_2 during selenation. By increasing the selenation temperature to 500 ^oC, the pure phase of $MoSe_2$ (JCPDS card No. 77-1715) appears as shown in **Figure 1h** (black line). By annealing MoO_3/CC at 550 ^oC for 3 h without the Se powder precursor, the pure phase of MoO_2/CC (JCPDS card No. 32-0671) is formed as shown by the blue line in **Figure 1h**. Pure MoO_2 cannot be obtained at a lower annealing temperature (450 ^oC, 6 h) or in a shorter time duration (550 ^oC, 2 h) as shown in **Figure S7**, suggesting that the Se powder precursor is important to the conversion of MoO_3 into MoO_2. The products are investigated by Raman scattering as shown in **Figure 1i**, which confirms the composite of MoO_2 and 1*T*-$MoSe_2$ [45]. **Figure 1j** indicates that conversion from MoO_3/CC to MoO_2/CC improves the electrical conductivity, but the pure selenide $MoSe_2$/CC product shows lower electrical conductivity. It has been reported that 1*T*-$MoSe_2$ shows excellent electrocatalytic activity in HER [42] and therefore, combining the highly active 1*T*-$MoSe_2$ with a highly conductive skeleton may enhance the catalytic capability. The electrical conductivity of the core-shell structure of MSM/CC is about six times larger than that of the pure phase $MoSe_2$/CC as well as superior to the MoO_3/CC precursor, as indicated in **Figure 1j**. The synergetic effects of high active site exposure and electrical conductivity of the MSM/CC composite are expected to benefit HER.

The chemical composition of the electrocatalysts was investigated by X-ray photoelectron spectroscopy (XPS). The selenide products including MSM/CC and $MoSe_2$/CC show the presence of Se in the surface survey in **Figure S8**. The high-resolution XPS spectra of Se 3*d*

in **Figures S9a-b** show similar spectra for the selenide samples and the peaks at 55.7/54.8 eV is Se^{2-} $3d_{3/2}/3d_{5/2}$. However, the Mo 3*d* spectra of MSM/CC, MoO_2/CC and $MoSe_2$/CC are different as shown in **Figures S10a-c**. MoO_2/CC is composed of Mo^{4+} (233.2 and 230.0 eV) and Mo^{6+} (235.6 and 232.1 eV) as shown by the Mo 3*d* spectra (**Figure S10a**). The presence of Mo^{6+} in MoO_2/CC stems from surface oxidation in air as reported before [46]. **Figures S10b-c** show that the Mo 3*d* peak in MSM/CC and $MoSe_2$/CC is composed of Mo^{4+} $3d_{3/2}$ and $3d_{5/2}$. The Mo^{4+} peaks in MSM/CC are shifted ~0.56 eV lower compared to MoO_2/CC, but ~0.20 eV higher than $MoSe_2$/CC. The peak shifts reveal the electronic interactions between the MoO_2 and $MoSe_2$ phases at the MSM heterointerface.

The electrochemical properties of the electrocatalysts were studied systematically based on the three-electrode configuration. **Figure 2a** depicts the polarization curves of the electrocatalysts in the alkaline electrolyte (1.0 M KOH) for HER. The MSM/CC electrocatalyst requires only 181 mV for a current density of 10 mA cm^{-2}, which is a common criterion to evaluate the activity of water splitting. The overpotential of the MSM/CC electrocatalyst is smaller than those of the pure phase of $MoSe_2$/CC (216 mV), MoO_2/CC (358 mV) and MoO_3/CC (363 mV), as listed in **Table S1**. Moreover, the MSM/CC electrocatalyst exhibits a rapid rise in the current density and an overpotential of 449 mV is needed to generate a large current density of 500 mA cm^{-2}. **Figure 2b** shows the Tafel slope of the electrocatalysts. The smallest Tafel slope of 110.4 mV dev^{-1} is observed from the MSM/CC electrocatalyst compared to the pure phase of $MoSe_2$/CC (133.6 mV dev^{-1}), MoO_2/CC (117.6 mV dev^{-1}), and MoO_3/CC (385.8 mV dev^{-1}). A smaller Tafel slope normally implies accelerated mass transport and charge transfer, which can be confirmed by electrochemical impedance spectroscopy (EIS) in **Figure 2c**. The smaller charge transfer resistance of MSM/CC suggests fast charge transfer in HER due to the tight combination of the $MoSe_2$ shell and highly conductive MoO_2 core.

Density-functional theory calculation (**Supporting Note 1**) was performed to elucidate the mechanism of the MSM/CC heterostructure. The simulated model for the MSM composed of

$MoSe_2$(002) and MoO_2(–211) heterointerface is depicted in **Figure S11a**. The calculated ΔG_H of $MoSe_2$, MoO_2, and MSM heterointerface was adopted to estimate the hydrogen evolution activity, as shown in **Figure S11b**. MSM shows a ΔG_H of –0.18 eV, which is closer to zero compared to pure $MoSe_2$ (–0.24 eV) and MoO_2 (0.54 eV), indicating that the interaction between $MoSe_2$ and MoO_2 at the heterointerface regulates the electronic structure of the active center to accelerate HER.

The electrochemically active surface area (ECSA) was derived to evaluate active site exposure based on cyclic voltammetry (**Figure S12**). The larger the ECSA, the greater is the active site exposure. As shown in **Figure 2d**, the MSM/CC electrocatalyst has the largest ECSA of 80.6 mF cm^{-2}, which is about 10 times that of the MoO_3/CC precursor, suggesting more active site exposure after phase separation. The results are supported by the SEM images after selenation showing that the surface of the nanowire becomes rough and sheet-like so that more active sites are exposed. The smaller overpotential, Tafel slope, and charge transfer resistance, as well as the larger ECSA of the MSM/CC electrocatalyst confirm the promotional effect of the $MoSe_2$ and MoO_2 heterostructure. The outstanding HER performance should be ascribed to the modulated electronic structure of the heterointerface between the two phases and the synergistic effects of highly active $MoSe_2$ and conductive MoO_2.

The HER capability of the MSM/CC electrocatalyst in electrolytes with a universal pH range was investigated and shown in **Figures 2e-f** and the overpotentials and Tafel slopes are listed in **Table S2**. The MSM/CC electrocatalyst needs both smaller overpotentials and Tafel slope in the acidic electrolyte (0.5 M H_2SO_4) than in the alkaline medium. The HER performance of the MSM/CC electrocatalyst in a neutral electrolyte (0.5 M Na_2SO_4) was studied and an overpotential of 568 mV was required for 10 mA cm^{-2}, together with a Tafel slope of 174.6 mV dec^{-1}. Generally, the HER characteristics in neutral media are inferior to those in acidic and alkaline media, but it is more practical to produce hydrogen in neutral electrolytes due to less electrode damage and equipment corrosion. The MSM/CC

electrocatalyst shows a more rapid rise in the current density throughout the applied potential range than the commercial Pt/C catalyst, as indicated in **Figure 2g**. The overpotentials required to produce a current density beyond 45 mA cm^{-2} are even smaller compared to the commercial catalyst. The HER characteristics of the MSM/CC electrocatalyst and other typical transition metal-based electrocatalysts in neutral electrolytes are compared in **Figure 2h** and the former indeed delivers outstanding performance.

Figure 2i shows the stability of the MSM/CC electrocatalyst in the neutral electrolyte and the catalyst worked stably for more than 75 h without obvious decay in the current density. Moreover, the morphology of the MSM/CC electrocatalyst remains the same and the nanosheets cover the nanowire arrays (**Figure S13**). **Figure S14** shows similar diffraction patterns from the MSM/CC electrocatalyst after a long-term test, compared to the fresh one, implying high stability. The amount of H_2 produced by the MSM/CC electrocatalyst in HER under the neutral condition is measured by the water displacement configuration as schematically illustrated in **Figure 2j**. The volume of hydrogen collected is determined by a measuring cylinder (100 mL) and 60.5 mL of hydrogen is produced after HER for 80 min at a constant current density of 100 mA cm^{-2}. High-purity hydrogen is emitted from the neutral electrolyte at a fast rate of 1.85 mmol h^{-1} (**Figure 2k**). In addition, the Faradaic efficiency is calculated to be as high as 99.58% (**Supporting Note 2**) corroborating the high efficiency in the neutral medium.

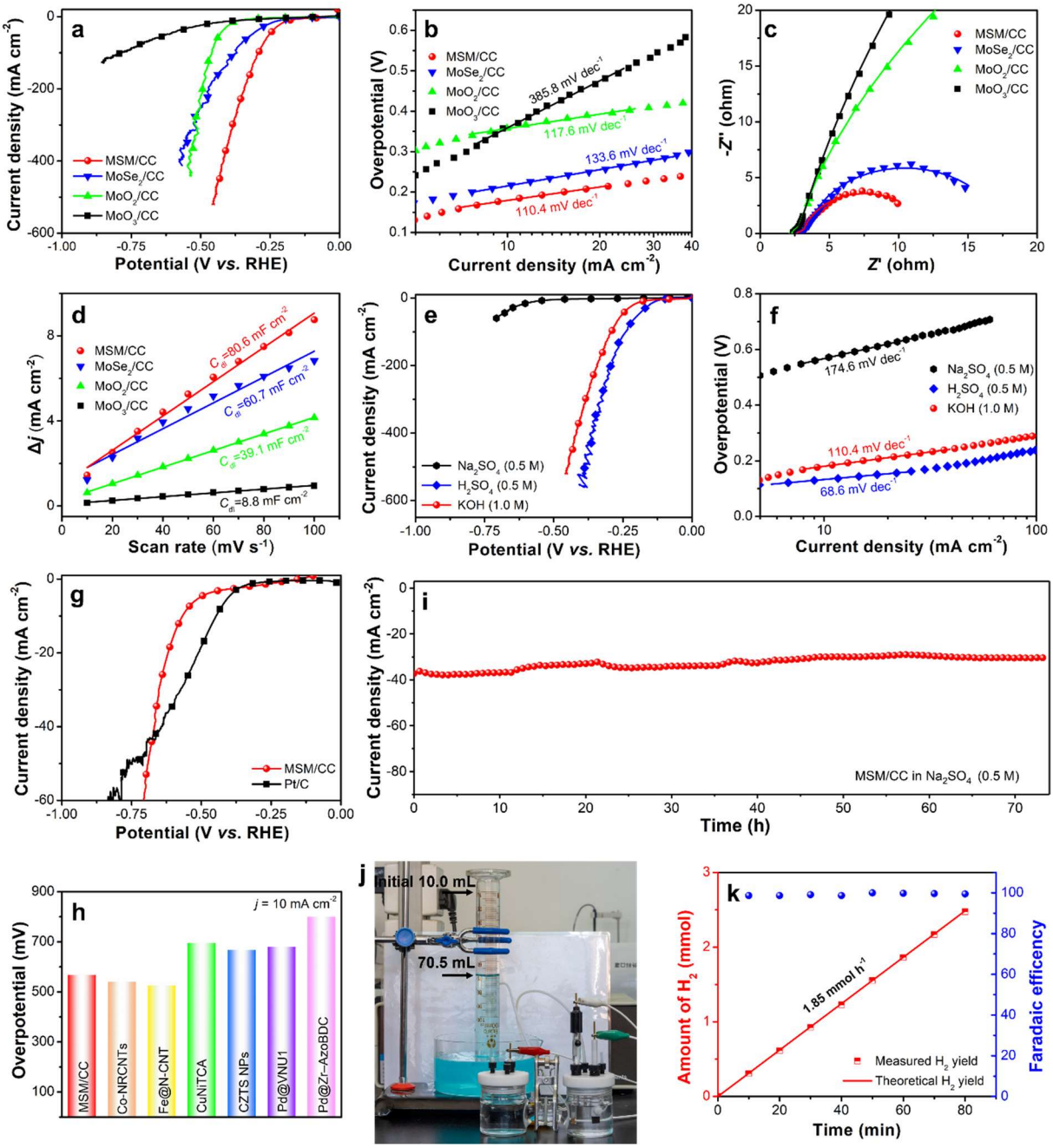

Figure 2. (a) Polarization curves, (b) Tafel slopes, (c) EIS, and (d) ECSA of the electrocatalysts measured in 1.0 M KOH electrolyte; (e) Polarization curves and (f) Tafel slopes of the MSM/CC electrocatalyst in different electrolytes; (g) Polarization curves of MSM/CC and commercial Pt/C electrocatalysts in 0.5 M Na_2SO_4; (h) Comparison of the overpotentials of MSM/CC with those of previously reported electrocatalysts in neutral electrolytes, including Fe@N-CNT [22], CuNiTCA [47], Co-NRCNTs [48], CZTS NPs [49], Pd@VNU1 [50], Pd@Zr-AzoBDC [51]; (i) Stability of MSM/CC in 0.5 M Na_2SO_4; (j) Photograph of the HER system with the MSM/CC electrocatalyst and H_2 gas generation determined by the water

displacement method; (k) Experimental and theoretical amounts of H_2 produced by the MSM/CC electrocatalyst and Faradaic efficiency at 100 mA cm^{-2}.

Since Fe corrodes easily and even self-corrodes in the electrolyte, during which both the anodic and cathodic reactions will occur spontaneously at the electrode surface, and as a result the electrode potential will be different from the reversible or equilibrium potential of each reaction occurring at the surface. In this case, the corrosion potential of Fe is intermediate between the equilibrium potential of the two half-reactions, as indicated by the open circuit potential (also called corrosion potential) measurement in **Figure S15**. Iron-based species have been investigated as OER electrocatalysts and reconstruction by oxidizing to higher valance states occurs before OER. That is, the FUR is more thermodynamic favorable than the OER. More importantly, waste steel in the construction industry can be recycled to be used as Fe electrodes instead of fresh smelting to reduce the cost, energy consumption, and carbon emission. Here, a waste steel rod (**Figure S16**) is used as the Fe electrode to determine the FOR properties. The polarization curve in **Figure 3a** shows that merely 0.11 V *vs*. RHE is required to generate a current density of 10 mA cm^{-2} in FUR in the neutral electrolyte (0.5 M Na_2SO_4), which is 2.01 V smaller than that in OER and even 1.71 V smaller than that of the commercial IrO_2 electrocatalyst (**Figure 3a** and **Figure S17**). The results show that by replacing OER with FUR, the energy consumption by the anodic reaction can decrease by 95%. During FUR, white flocculent precipitates are formed as shown in **Figure S18a**. To analyze the product of FUR, the final electrolyte after FUR was put in a $KMnO_4$ aqueous solution. The purple $KMnO_4$ solution turns to clay-bank as shown in **Figures S18b-c**, suggesting that Fe(II) is produced in FUR due to electrochemical oxidation of the Fe electrode, which is consistent with the literature [22]. The results predict that combining HER and FUR can give rise to energy-saving hydrogen production with hydrogen being the only gaseous product together with other value-adding by-products.

To assess the practicability of the HER/FUR strategy for hydrogen production, the overall reaction of HER and FUR using the MSM/CC electrocatalyst and waste steel rod as electrodes was carried out, as shown in **Figure 3b**. The polarization curve acquired in the neutral electrolyte (0.5 M Na_2SO_4) is presented in **Figure 3c**. The voltage required by the MSM/CC-Fe couple is smaller than that of the commercial Pt/C-IrO_2 couple. In detail, a voltage of 0.68 V is needed to generate a current density of 10 mA cm^{-2} for the MSM/CC-Fe couple in the neutral electrolyte and it is superior to those of the HER/OER couple in acidic and basic electrolytes, as listed in **Table S3**. The faraday efficiency of the HER/FUR overall configuration for H_2 production was calculated to be 99.5% in an electrolyzer without a separator as shown in **Figure S19a-b,** which suggested that the reactants and products of the redox reactions occurring on the cathode and anode do not interact with each other. The evaluation of the stability and feasibility of the HER/FUR integrated system in **Figure S20** shows a slight decay of the current density after continuous testing for 24 h, which can be ascribed to the consumption of the Fe anode since the current density returns to the initial state after Fe electrode replacement. The precipitated floccule (after washing and drying) formed in HER/FUR was studied by FE-SEM and XRD revealing nanosized Fe_3O_4 (JCPDS card No. 75-0033) particles (**Figure 3d** and **Figure S21**), resulting from partial oxidation of Fe(II) since it is generally unstable and prefers to be oxidized. Moreover, the magnetic properties of the as-obtained Fe_3O_4 nanoparticles and commercial Fe_3O_4 were investigated and shown in **Figure 3e**. The magnetic hysteresis loop shows no remanence or coercivity at room temperature, thus indicating that the nanosized particles have superparamagnetic characteristics. The as-obtained Fe_3O_4 nanoparticles and commercial Fe_3O_4 particles have magnetic saturation (MS) values of approximately 52.0 and 2.6 emu g^{-1}, respectively, suggesting superior magnetic properties for the as-obtained Fe_3O_4 nanoparticles. In addition, the final Fe product can be picked up by a magnet as shown in the inset in **Figure 3e**, suggesting promising magnetic applications. Generally, the nanosized magnetic powder is more valuable than the waste steel rod at the anode

and therefore, the anodic reaction is value-adding and should further reduce the cost of hydrogen production. Furthermore, the electricity requirement for the HER/FUR couple in the neutral electrolyte is calculated to be 2.69 kWh per m^3 H_2 (**Supporting Note 3**). More importantly, high-purity hydrogen and value-adding Fe_3O_4 nanoparticles are produced in conjunction with zero carbon emission. It is lower than that of common overall water splitting systems and even less than the theoretical limit of conventional overall water splitting (2.94 kWh per m^3 H_2), as shown in **Figure 3f**.

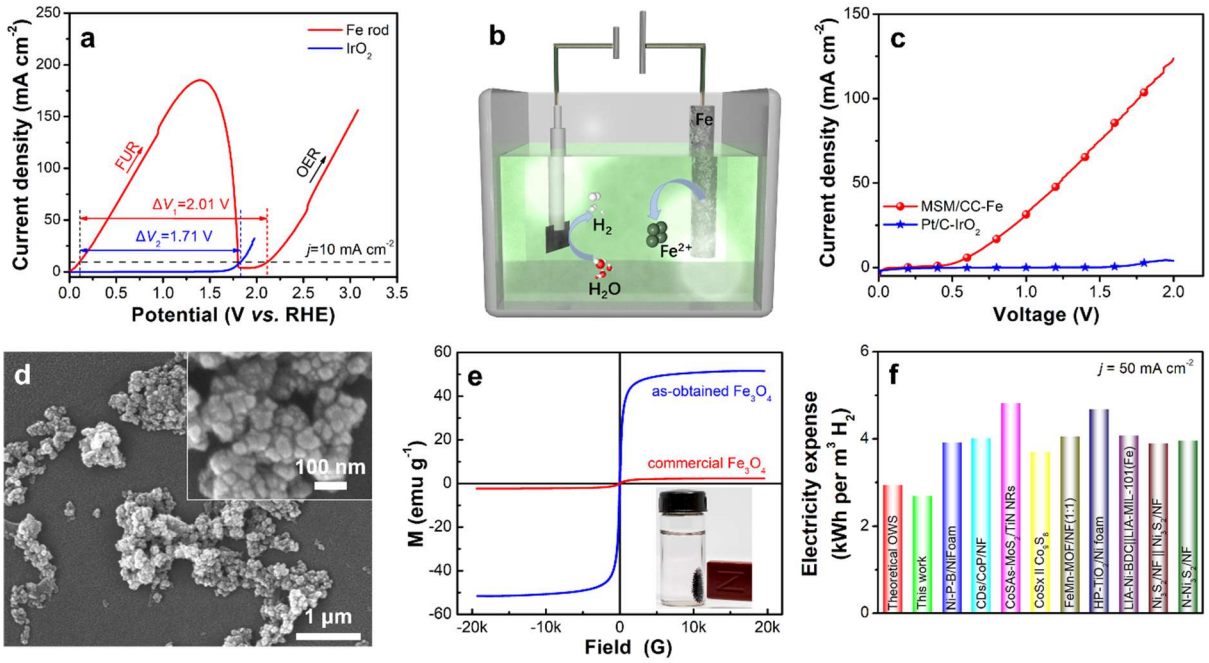

Figure 3. (a) LSV curves of FUR with a waste steel rod as the working electrode; (b) Model of the HER/FUR couple; (c) LSV curves of MSM/CC-Fe and Pt/C-IrO_2 couples; (d) SEM images and (e) Magnetic properties of the as-obtained Fe_3O_4; (f) Comparison of the energy requirement of the HER/FUR overall reaction system in this work with those of theoretical overall water splitting and reported works, including Ni-P-B/Ni foam [52], CDs/CoP/NF [53], CoSAs-MoS_2/TiN NRs [54], CoS_x||Co_9S_8 [55], FeMn-MOF/NF(1:1) [56], HP-TiO_2/Ni foam [57], LIA-Ni-BDC||LIA-MIL-101(Fe) [58], Ni_3S_2/NF||Ni_3S_2/NF [59], and N-Ni_3S_2/NF [60].

Coupling FUR and HER enables energy-saving hydrogen production but FUR consumes Fe. To further increase the economic benefits of HER/FUR, the product can be used to extract RhB from polluted water *via* flocculation, a process commonly used in environmental fields to remove pollutants including heavy metal ions and organic species from neutral wastewater. After adding RhB into the neutral electrolyte, the polarization curves for the HER and HER/FUR overall reaction remain the same, as shown in **Figure S22**. During the HER/FUR overall reaction, the color of the electrolyte changes from rose red to garnet accompanied by floccule formation. The electrolyte then turns colorless and precipitates are formed as shown in **Figure 4a**. The precipitation process is shown in the **Supporting Video** which shows that bubbles are emitted from the cathode and floccule precipitates in the electrolyte in HER/FUR. **Figure 4b** shows the schematic of recovery of polluted water and formation of value-adding products in the process. RhB-containing wastewater can be purified by the HER/FUR overall reaction, as indicated by the fact that the total organic carbon (TOC) decreases from 167.9 to 19.5 mg L^{-1} (**Figure S23**). At the same time, RhB can be recovered from the electrolyte by coagulation of the floccule. The UV-vis spectra of the electrolyte during the overall reaction are shown in **Figure 4c**, which indicates that RhB can be removed completely after the reaction in ~30 min. The UV-vis spectra of coagulated electrolyte indicate the same peak location to the initial one but the absorbance increases by 80% as shown in **Figure 4d**, suggesting the RhB is beneficiated to a higher concentration. The results reveal that the chemistry of RhB remains unchanged through floccule precipitation, during which RhB can be beneficiated. Furthermore, the HER/FUR overall reaction can be powered by a solar cell with an output voltage of 1.5 V as illustrated in **Figure 4e**. Bubbles are generated from the MSM/CC electrode only as shown in **Figures 4f-g**. The results indicate that energy-saving hydrogen production can be realized in conjunction with RhB recovery from polluted water in one system powered by sustainable energy.

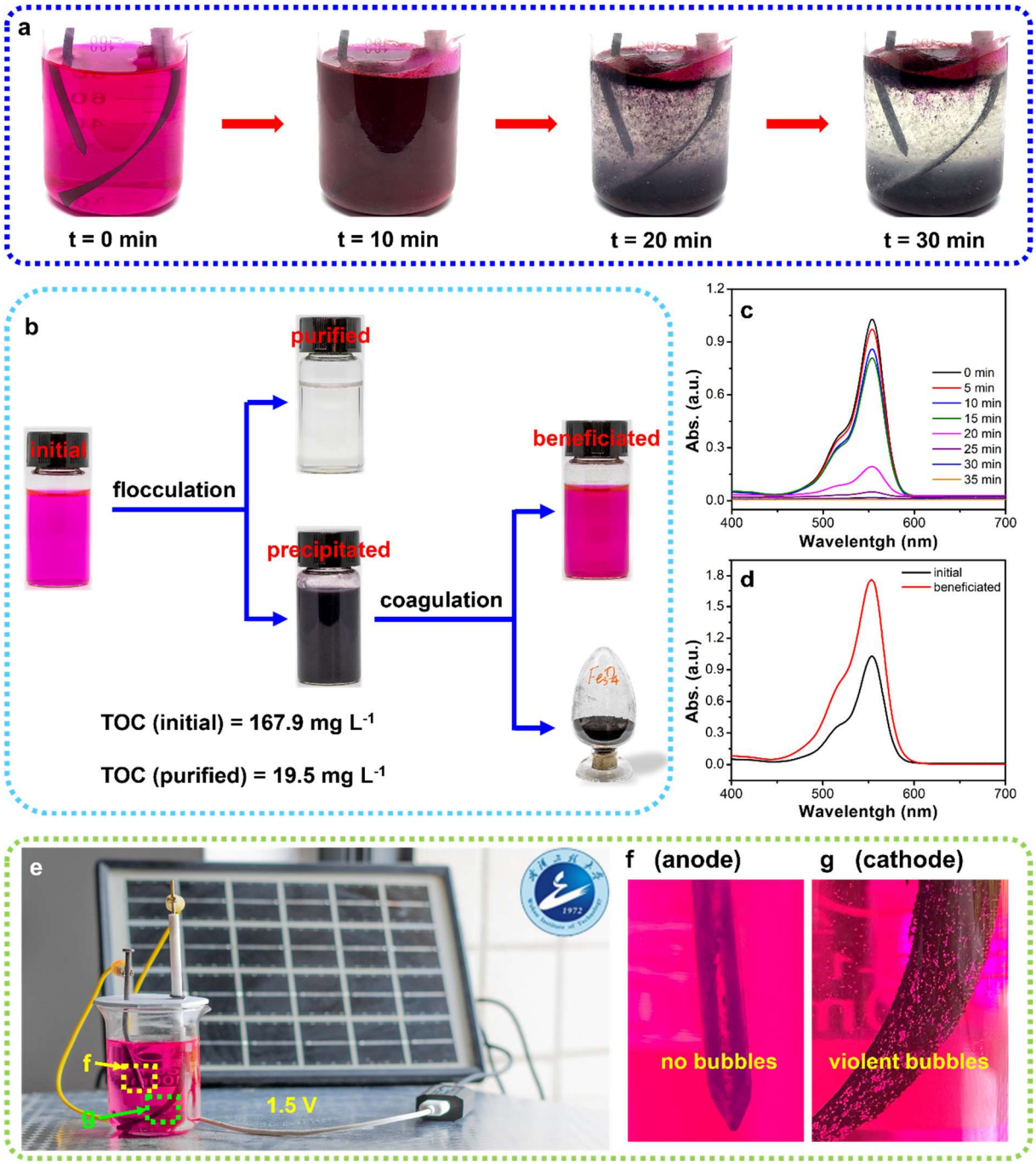

Figure 4. (a) Pictures of the HER/FUR electrolyte in different states; (b) Schematic of polluted water recovery and formation of value-adding products; (c) UV-vis spectra of the electrolyte (6 times dilution) during the HER/FUR overall reaction; (d) UV-vis spectra of the fresh electrolyte and beneficiated RhB with 6 times dilution; (e) Photograph showing the solar cell-powered HER/FUR overall reaction system; Photographs of (f) Anode and (g) Cathode in the HER/FUR reaction.

The RhB beneficiation process and mechanism are described in the **Supporting Note**. Firstly, the Fe rod is oxidized into Fe^{2+} on the anode in the reaction. Owing to the small *K*sp (solubility product constant) of $Fe(OH)_2$, Fe^{2+} prefers to form a nanosized $Fe(OH)_2$ precipitate in the neutral electrolyte (0.5 M Na_2SO_4, pH = 5.80) as described in the **Supporting Note 4**. Secondly, the RhB molecules adsorb onto the $Fe(OH)_2$ and precipitate with it. As a result, RhB is extracted from the polluted electrolyte and the resulting concentration diminishes. Generally, Fe(II) is unstable and prefers to be oxidized. Thirdly, by means of separation of the $Fe(OH)_2$ and RhB by coagulation, the adsorbed RhB is released into the solution to form the beneficiated solution. At the same time, $Fe(OH)_2$ is precipitated and sinks to the bottom. In the full cycle of absorption and release of the RhB, only electrostatic adsorption works and therefore, RhB can be beneficiated without chemical evolution. Therefore, the FUR coupled HER overall reaction not only decreases the energy consumption of hydrogen production intrinsically but also beneficiates RhB from polluted water for recycling. Moreover, magnetic Fe_3O_4 nanoparticles are produced from the waste steel rod, as analyzed in **Supporting Note 5**. The process accomplishes clean energy production and environmental recovery at the same time while emitting zero carbon.

4. Conclusion

A novel strategy to integrate HER and FUR is demonstrated for simultaneous energy-saving hydrogen production and organic pollutant removal/recovery in neutral media. High-purity hydrogen is produced on the cathode electrocatalyzed by a heterostructured MSM/CC electrocatalyst, which requires 568 mV to generate a current density of 10 mA cm^{-2} and shows a Tafel slope of 174.6 mV dec^{-1} in 0.5 M Na_2SO_4. The outstanding HER capability in the neutral electrolyte originates from the synergetic effects of high active site exposure and electrical conductivity of the MSM/CC heterostructure. Owing to the favorable thermodynamics of FUR compared to OER, the potential required to achieve an anodic current

density of 10 mA cm^{-2} decreases by 95%. Additionally, the HER/FUR couple requires 0.68 V to achieve 10 mA cm^{-2} and can thus be powered by solar cells. The electricity equivalent of the HER/FUR couple in the neutral electrolyte is calculated to be 2.69 kWh per m^3 H_2 for the production of high-purity hydrogen with zero carbon emission. The waste steel rod used as the anode is oxidized into Fe^{2+}, which can be used to extract RhB from wastewater. As a result, purified water with extremely low TOC has been obtained. The beneficiated RhB has been separated from the electrolyte by the following coagulation of Fe species. In addition, value-adding Fe_3O_4 magnetic powder with superparamagnetic characteristics and high magnetic saturation value is also formed. Our work reveals a new way to realize energy-efficient hydrogen production and environmental recovery and the strategy is promising for carbon-neutral energy and ecological systems.

Conflict of interest

The authors declare that they have no conflict of interest.

Acknowledgements

This work was financially supported by the Key Research and Development Program of Hubei Province (2021BAA208), National Natural Science Foundation of China (52002294, 51974208 and U2003130), Outstanding Youth Foundation of Natural Science Foundation of Hubei Province (2020CFA099), Young Top-notch Talent Cultivation Program of Hubei Province, Knowledge Innovation Program of Wuhan-Shuguang Project (2022010801020364), City University of Hong Kong Strategic Research Grant (SRG) (7005505), Shenzhen-Hong Kong Innovative Collaborative Research and Development Program (SGLH20181109110802117 and CityU 9240014), and City University of Hong Kong Donation Research Grant (DON-RMG 9229021).

Author contributions

Zhitian Liu, Biao Gao, and Paul K Chu supervised and conceived this project. Xiang Peng, Song Xie, Shijian Xiong, Rong Li, and Peng Wang carried out materials fabrication, materials characterizations, electrochemical measurements, and DFT calculations. Xiang Peng, Xuming Zhang, and Liangsheng Hu analyzed the results and wrote the paper. Xiang Peng, Zhitian Liu, Biao Gao, and Paul K Chu revised the manuscript and triggered helpful discussion. All authors discussed the results and commended the manuscript.

Appendix A. Supplementary materials

Supplementary materials to this article can be found online at

References

[1] Turner JA. Sustainable hydrogen production. Science 2004; 305: 972-4.

[2] Dresselhaus MS, Thomas I. Alternative energy technologies. Nature 2001; 414: 332-7.

[3] Su J, Zhou J, Wang L, et al. Synthesis and application of transition metal phosphides as electrocatalyst for water splitting. Sci Bull 2017; 62: 633-44.

[4] Zhao G, Jiang Y, Dou S-X, et al. Interface engineering of heterostructured electrocatalysts towards efficient alkaline hydrogen electrocatalysis. Sci Bull 2021; 66: 85-96.

[5] Li Y, Zhou L, Guo S. Noble metal-free electrocatalytic materials for water splitting in alkaline electrolyte. EnergyChem 2021; 3: 100053.

[6] Song W, Li M, Wang C, et al. Electronic modulation and interface engineering of electrospun nanomaterials-based electrocatalysts toward water splitting. Carbon Energy 2021; 3: 101-28.

[7] Zhang B, Wang L, Cao Z, et al. High-valence metals improve oxygen evolution reaction performance by modulating 3d metal oxidation cycle energetics. Nat Catal 2020; 3: 985-92.

[8] Li J, Zhang C, Zhang C, et al. Green electrosynthesis of 5, 5'-azotetrazolate energetic materials plus energy-efficient hydrogen production using ruthenium single-atom catalysts. Adv Mater 2022: 2203900.

[9] Li Y, Zhang J, Liu Y, et al. Partially exposed RuP_2 surface in hybrid structure endows its bifunctionality for hydrazine oxidation and hydrogen evolution catalysis. Sci Adv 2020; 6: eabb4197.

[10] Liu Y, Zhang J, Li Y, et al. Manipulating dehydrogenation kinetics through dual-doping Co_3N electrode enables highly efficient hydrazine oxidation assisting self-powered H_2 production. Nat Commun 2020; 11: 1853.

[11] Zhao H, Lu D, Wang J, et al. Raw biomass electroreforming coupled to green hydrogen generation. Nat Commun 2021; 12: 2008.

[12] Wang T, Tao L, Zhu X, et al. Combined anodic and cathodic hydrogen production from aldehyde oxidation and hydrogen evolution reaction. Nat Catal 2022; 5: 66-73.

[13] Sun H, Li L, Chen H-C, et al. Highly efficient overall urea electrolysis via single-atomically active centers on layered double hydroxide. Sci Bull 2022; 67: 1763-75.

[14] Qian Q, Zhang J, Li J, et al. Artificial heterointerfaces achieve delicate reaction kinetics towards hydrogen evolution and hydrazine oxidation catalysis. Angew Chem Int Ed 2021; 60: 5984-93.

[15] Qin H, Ye Z, Wei X, et al. Bifunctional electrolyzation for simultaneous organic pollutant degradation and hydrogen generation. ACS ES&T Eng 2021; 1: 1360-8.

[16] Zhao B, Liu J, Feng R, et al. Less-energy consumed hydrogen evolution coupled with electrocatalytic removal of ethanolamine pollutant in saline water over $Ni@Ni_3S_2$/CNT nano-heterostructured electrocatalysts. Small Methods 2022; 6: 2101195.

[17] Zhang L, Wang Z, Qiu J. Energy-saving hydrogen production by seawater electrolysis coupling sulfion degradation. Adv Mater 2022; 34: 2109321.

[18] Sun F, Qin J, Wang Z, et al. Energy-saving hydrogen production by chlorine-free hybrid seawater splitting coupling hydrazine degradation. Nat Commun 2021; 12: 4182.

[19] Huang C, Miao X, Pi C, et al. Mo_2C/VC heterojunction embedded in graphitic carbon network: An advanced electrocatalyst for hydrogen evolution. Nano Energy 2019; 60: 520-6.

[20] Peng X, Jin X, Liu N, et al. A high-performance electrocatalyst composed of nickel clusters encapsulated with a carbon network on TiN nanaowire arrays for the oxygen evolution reaction. Appl Surf Sci 2021; 567: 150779.

[21] Peng X, Yan Y, Jin X, et al. Recent advance and prospectives of electrocatalysts based on transition metal selenides for efficient water splitting. Nano Energy 2020; 78: 105234.

[22] Yu J, Li G, Liu H, et al. Electrochemical flocculation integrated hydrogen evolution reaction of Fe@ N-doped carbon nanotubes on iron foam for ultralow voltage electrolysis in neutral media. Adv Sci 2019; 6: 1901458.

[23] Aramaki K, Shimura T. An ultrathin polymer coating of carboxylate self-assembled monolayer adsorbed on passivated iron to prevent iron corrosion in 0.1M Na_2SO_4. Corros Sci 2010; 52: 1-6.

[24] Zhang Z, Chen S, Li Y, et al. A study of the inhibition of iron corrosion by imidazole and its derivatives self-assembled films. Corros Sci 2009; 51: 291-300.

[25] McCrum IT, Koper M. The role of adsorbed hydroxide in hydrogen evolution reaction kinetics on modified platinum. Nat Energy 2020; 5: 891-9.

[26] Zhou KL, Wang Z, Han CB, et al. Platinum single-atom catalyst coupled with transition metal/metal oxide heterostructure for accelerating alkaline hydrogen evolution reaction. Nat Commun 2021; 12: 1-10.

[27] He Q, Tian D, Jiang H, et al. Achieving efficient alkaline hydrogen evolution reaction over a Ni_5P_4 catalyst incorporating single-atomic Ru sites. Adv Mater 2020; 32: 1906972.

[28] Zhu CR, Gao D, Ding J, et al. TMD-based highly efficient electrocatalysts developed by combined computational and experimental approaches. Chem Soc Rev 2018; 47: 4332-56.

[29] Peng X, Hu L, Wang L, et al. Vanadium carbide nanoparticles encapsulated in graphitic carbon network nanosheets: A high-efficiency electrocatalyst for hydrogen evolution reaction. Nano Energy 2016; 26: 603-9.

[30] Qiang M, Zhang X, Song H, et al. General synthesis of nanostructured Mo_2C electrocatalysts using a carbon template for electrocatalytic applications. Carbon 2022; 197: 238-45.

[31] Peng X, Qasim AM, Jin W, et al. Ni-doped amorphous iron phosphide nanoparticles on TiN nanowire arrays: An advanced alkaline hydrogen evolution electrocatalyst. Nano Energy 2018; 53: 66-73.

[32] Yang M, Shang C, Li F, et al. Synergistic electronic and morphological modulation on ternary $Co_{1-x}V_xP$ nanoneedle arrays for hydrogen evolution reaction with large current density. Sci China Mater 2021; 64: 880-91.

[33] Lee YH, Zhang XQ, Zhang W, et al. Synthesis of large-area MoS_2 atomic layers with chemical vapor deposition. Adv Mater 2012; 24: 2320-5.

[34] Xie L, Wang L, Zhao W, et al. WS_2 moiré superlattices derived from mechanical flexibility for hydrogen evolution reaction. Nat Commun 2021; 12: 5070.

[35] Zang W, Sun T, Yang T, et al. Efficient hydrogen evolution of oxidized Ni-N3 defective sites for alkaline freshwater and seawater electrolysis. Adv Mater 2021; 33: 2003846.

[36] Peng X, Pi C, Zhang X, et al. Recent progress of transition metal nitrides for efficient electrocatalytic water splitting. Sustain Energ Fuels 2019; 3: 366-81.

[37] Chen J, Pan A, Zhang W, et al. Melamine-assisted synthesis of ultrafine Mo_2C/Mo_2N@ N-doped carbon nanofibers for enhanced alkaline hydrogen evolution reaction activity. Sci China Mater 2021; 64: 1150-8.

[38] Peng X, Yan Y, Xiong S, et al. Se-$NiSe_2$ hybrid nanosheet arrays with self-regulated elemental Se for efficient alkaline water splitting. J Mater Sci Technol 2022; 118: 136-43.

[39] Peng X, Xie S, Wang X, et al. Energy-saving hydrogen production by methanol oxidation reaction coupled hydrogen evolution reaction co-catalyzed by phase separation induced heterostructure. J Mater Chem A 2022; 10: 20761-9.

[40] Xia B, Wang T, Jiang X, et al. Ar^{2+} beam irradiation-induced multivancancies in $MoSe_2$ nanosheet for enhanced electrochemical hydrogen evolution. ACS Energy Lett 2018; 3: 2167-72.

[41] Deng S, Zhong Y, Zeng Y, et al. Directional construction of vertical nitrogen-doped 1T-2H $MoSe_2$/graphene shell/core nanoflake arrays for efficient hydrogen evolution reaction. Adv Mater 2017; 29: 1700748.

[42] Chang L, Sun Z, Hu YH. 1T phase transition metal dichalcogenides for hydrogen evolution reaction. Electrochem Energy R 2021; 4: 194-218.

[43] Qu Y, Medina H, Wang SW, et al. Wafer scale phase-engineered 1T-and 2H-$MoSe_2$/Mo core-shell 3D-hierarchical nanostructures toward efficient electrocatalytic hydrogen evolution reaction. Adv Mater 2016; 28: 9831-8.

[44] Deng S, Ai C, Luo M, et al. Coupled biphase (1T-2H)-$MoSe_2$ on mold spore carbon for advanced hydrogen evolution reaction. Small 2019; 15: 1901796.

[45] Gupta U, Naidu B, Maitra U, et al. Characterization of few-layer 1T-$MoSe_2$ and its superior performance in the visible-light induced hydrogen evolution reaction. APL Mater 2014; 2: 092802.

[46] Lu X-F, Huang Z-X, Tong Y-X, et al. Asymmetric supercapacitors with high energy density based on helical hierarchical porous Na_xMnO_2 and MoO_2. Chem Sci 2016; 7: 510-7.

[47] Vishwanath RS, Kandaiah S. Metal ion-containing $C_3N_3S_3$ coordination polymers chemisorbed to a copper surface as acid stable hydrogen evolution electrocatalysts. J Mater Chem A 2017; 5: 2052-65.

[48] Zou X, Huang X, Goswami A, et al. Cobalt-embedded nitrogen-rich carbon nanotubes efficiently catalyze hydrogen evolution reaction at all pH values. Angew Chem Int Ed 2014; 53: 4372-6.

[49] Digraskar RV, Mulik BB, Walke PS, et al. Enhanced hydrogen evolution reactions on nanostructured Cu_2ZnSnS_4 (CZTS) electrocatalyst. Appl Surf Sci 2017; 412: 475-81.

[50] Le HV, Le Doan TH, Tran BQ, et al. Selective incorporation of Pd nanoparticles into the pores of an alkyne-containing metal-organic framework VNU1 for enhanced electrocatalytic hydrogen evolution reaction at near neutral pH. Mater Chem Phys 2019; 233: 16-20.

[51] Le HV, Nguyen QTT, Co TT, et al. A composite based on Pd nanoparticles incorporated into a zirconium-based metal-organic frameworks Zr-AzoBDC and its electrocatalytic activity for hydrogen evolution reaction. J Electron Mater 2018; 47: 6918-22.

[52] Hao W, Wu R, Huang H, et al. Fabrication of practical catalytic electrodes using insulating and eco-friendly substrates for overall water splitting. Energy Environ Sci 2020; 13: 102-10.

[53] Zhang L-C, Chen H, Hou G-R, et al. Puzzle-inspired carbon dots coupled with cobalt phosphide for constructing a highly-effective overall water splitting interface. Chem Commun 2020; 56: 257-60.

[54] Doan TLL, Nguyen DC, Prabhakaran S, et al. Single-atom Co-decorated MoS_2 nanosheets assembled on metal nitride nanorod arrays as an efficient bifunctional electrocatalyst for pH-universal water splitting. Adv Funct Mater 2021; 31: 2100233.

[55] Souleymen R, Wang Z, Qiao C, et al. Microwave-assisted synthesis of graphene-like cobalt sulfide freestanding sheets as an efficient bifunctional electrocatalyst for overall water splitting. J Mater Chem A 2018; 6: 7592-607.

[56] Guan H, Wang N, Feng X, et al. FeMn bimetallic MOF directly applicable as an efficient electrocatalyst for overall water splitting. Colloids Surf, A 2021; 624: 126596.

[57] Yan Y, Cheng X, Zhang W, et al. Plasma hydrogenated TiO2/Nickel foam as an efficient bifunctional electrocatalyst for overall water splitting. ACS Sustain Chem Eng 2018; 7: 885-94.

[58] Tang YJ, Zheng H, Wang Y, et al. Laser-induced annealing of metal-organic frameworks on conductive substrates for electrochemical water splitting. Adv Funct Mater 2021; 31: 2102648.

[59] Luo X, Ji P, Wang P, et al. Interface engineering of hierarchical branched Mo-doped Ni_3S_2/Ni_xP_y hollow heterostructure nanorods for efficient overall water splitting. Adv Energy Mater 2020; 10: 1903891.

[60] Chen P, Zhou T, Zhang M, et al. 3D nitrogen-anion-decorated nickel sulfides for highly efficient overall water splitting. Adv Mater 2017; 29: 1701584.